ADVANCED FUNCTIONAL MATERIALS
www.afm-journal.de

# New Strategy for Polysulfide Protection Based on Atomic Layer Deposition of $TiO_2$ onto Ferroelectric-Encapsulated Cathode: Toward Ultrastable Free-Standing Room Temperature Sodium–Sulfur Batteries

*Dingtao Ma, Yongliang Li, Jingbo Yang, Hongwei Mi, Shan Luo, Libo Deng, Chaoyi Yan, Muhammad Rauf, Peixin Zhang,* Xueliang Sun,* Xiangzhong Ren, Jianqing Li, and Han Zhang*

**The room temperature (RT) sodium–sulfur batteries (Na–S) hold great promise for practical applications including energy storage and conversion due to high energy density, long lifespan, and low cost, as well based on the abundant reserves of both sodium metal and sulfur. Herein, freestanding (C/S/$BaTiO_3$)@$TiO_2$ (CSB@$TiO_2$) electrode with only ≈3 wt% of $BaTiO_3$ additive and ≈4 nm thickness of amorphous $TiO_2$ atomic layer deposition protective layer is rational designed, and first used for RT Na–S batteries. Results show that such cathode material exhibits high rate capability and excellent durability compared with pure C/S and C/S/$BaTiO_3$ electrodes. Notably, this CSB@$TiO_2$ electrode performs a discharge capacity of 524.8 and 382 mA h $g^{-1}$ after 1400 cycles at 1 A $g^{-1}$ and 3000 cycles at 2 A $g^{-1}$, respectively. Such superior electrochemical performance is mainly attributed from the "$BaTiO_3$-C-$TiO_2$" synergetic structure within the matrix, which enables effectively inhibiting the shuttle effect, restraining the volumetric variation and stabilizing the ionic transport interface.**

## 1. Introduction

The utilization of advanced, renewable, and low-cost energies has been greatly developed for satisfying the social requirements in the past decades. Among those potential candidates, sulfur-based batteries have been developed rapidly owing to the advantages of decent energy density, excellent sustainability, abundance storage, and low cost of sulfur sources. Notably, although the lithium–sulfur (Li–S) batteries has particular interest and hold potential to serve as next-generation rechargeable batteries due to their high theoretic specific capacity (1672 mA h $g^{-1}$) and energy density (2600 Wh $kg^{-1}$). However, the high cost of lithium metal also becomes one of the major obstacles for their commercialization on large scale.[1–4] With this regard, the development of room temperature (RT) sodium–sulfur (Na–S) batteries seems to be a good alternative since the abundant reserves and acceptable price of sodium metal. [5,6]

Similar to Li–S batteries, the intrinsic drawback such as poor electronic conductivity of sulfur ($5 \times 10^{-30}$ S $cm^{-1}$), dissolution of polysulfide intermediates and large volume expansion during cycling, would always decrease the utilization of active material and lead to a poor battery lifespan for RT Na–S batteries. So far, there are still only a few studies reported about the preventing of "shuttle effect," as well as the improvement of electrical conductivity of the S-based cathodes for building high performance RT Na–S batteries.[7–12] Generally, those strategies could be mainly summarized as follow: (1) coating sulfur with conductive polymers/carbon materials;[9,13] (2) infusing S into porous carbon matrix;[5,7,10,11,14–16] and (3) introducing other additive in electrode composition.[17–19] Among them, encapsulating S with porous carbon matrix becomes one of the promising approaches to tackle the abovementioned obstacles. Unfortunately, that carbon matrix with ultramicroporous ($d$ < 1 nm) structure always leads to a low sulfur loading and energy density.[10,14–16] On the other hand, it should be pointed out that the formation of C/S composite could not be enough to

D. T. Ma, Dr. Y. L. Li, J. B. Yang, Dr. H. W. Mi, S. Luo, Dr. L. B. Deng, Prof. C. Y. Yan, Dr. M. Rauf, Prof. P. X. Zhang, Prof. X. Z. Ren
College of Chemistry and Environmental Engineering
Shenzhen University
Shenzhen 518060, China
E-mail: pxzhang@szu.edu.cn
D. T. Ma, Prof. J. Q. Li, Prof. H. Zhang
Faculty of Information Technology
Macau University of Science and Technology
Macau 519020, China
D. T. Ma, Prof. H. Zhang
SZU-NUS Collaborative Innovation Center for Optoelectronic Science and Technology and Key Laboratory of Optoelectronic Devices and Systems of Ministry of Education and Guangdong Province
Shenzhen University
Shenzhen 518060, China
Prof. X. Sun
Department of Mechanical and Materials Engineering
University of Western Ontario
London, Ontario N6A 5B8, Canada
E-mail: xsun@eng.uwo.ca

DOI: 10.1002/adfm.201705537

 

tackle the "shuttle effect" during charge/discharge process due to the weak polar surface of the carbon matrix.[1,18–20] To end of this concern, other effective ways to inhibit the dissolution of intermediate polysulfide by forming the strong chemical bond with S species in RT Na–S system is still yet to be developed.

In this case, inspirations obtained from Li–S systems could be a wise choice since their similar construction with Na–S batteries. To date, various strategies with respect to addressing the polysulfide shuttle phenomenon in Li–S batteries have been widely explored. In addition to form the C/S composite mentioned above,[21,22] conductive polymers,[23–27] metal-based compounds (e.g., metal sulfides,[28–30] metal oxides,[31–37] and metal carbides[38–40]), modification of the separator,[41,42] and other effective ways,[43–46] were also applied and further demonstrated. Among them, metal oxide such as $TiO_2$,[30,31] $MnO_2$,[33,35] and $Fe_3O_4$[37] have been systemically demonstrated as promising host materials for S due to their strong polar surface. Previously, rational designed S-$TiO_2$ yolk-shell nanoparticles for Li–S batteries were reported by Cui and co-workers,[47] as electrode displayed an excellent stability with a Coulombic efficiency of 98.4% after 1000 cycles. Unlike the common host materials, Xie et al.[48] has proved that ferroelectric materials also useful to trap the polysulfide due to internal electric field originated from the spontaneous polarization recently. Although such host materials or ferroelectric materials enable greatly to improve the electrochemical performance of Li–S batteries. However, such nonelectrochemical active additives would not only decrease the energy density of batteries but also enhance the productive cost since their occupancies always exceed 10 wt% and even 20 wt%.[29,33,34,38] Considering the above questions, the rational design of electrode to obtain high energy density with low cost of Na–S batteries seems to be very necessary and meaningful in the future research.

In this work, we developed a new strategy for fabricating high energy density and long lifespan RT Na–S batteries based on the ferroelectric effect and atomic layer deposition (ALD) technique. Porous free-standing C/$BaTiO_3$ (denoted C/B) mats without any other conductive/binder additives can be directly obtained by electrospinning and subsequent carbonization process. By adding ≈3 wt% of commercial $BaTiO_3$ nanoparticles (a kind of common and cheap ferroelectric material with a characteristic of spontaneous polarization to form large electric dipole moments, which has been proved as an effective modification reagent in energy storage systems [48–50]), the C/S/$BaTiO_3$ electrode (denoted C/S/BTO) showed high performance than that of the pure C/S electrode. Based on this, ≈4 nm thickness of amorphous $TiO_2$ nanolayers were directly deposited on the surface of C/S/BTO electrode to get the (C/S/BTO)@$TiO_2$ (denoted CSB@$TiO_2$) electrode. The CSB@$TiO_2$ composite exhibited cyclic stability over 1400 and 3000 cycles while still remaining 524.8 and 382 mA h $g^{-1}$ at 1 and 2 A $g^{-1}$, respectively, showing a great potential in the future applications of RT Na–S batteries.

## 2. Results and Discussions

The schematic synthesis of (C/S/$BaTiO_3$)@$TiO_2$ electrode is illustrated in **Figure 1**a. First, the mixture of polyacryonitrile, F127 and $BaTiO_3$ nanoparticles (Figure S1a, Supporting Information) were added into the solvent of dimethylformamide to form the precursor for electrospinning. It should be pointed out that the triblock copolymer F127 was used as additive and it mainly played two important roles. On one hand, F127 as surfactant could effective enhance the dispersion of $BaTiO_3$ nanoparticles inside the carbon nanofibers. On the other hand, F127 as a soft template here would create nanoporous structure within carbon nanofibers.[51–53] Then C/$BaTiO_3$ and C/S/$BaTiO_3$ mats can be obtained after carbonization and following sulfur melt diffusion process, respectively. Finally, the CSB@$TiO_2$ electrode was prepared after $TiO_2$ ALD treatment with C/S/BTO electrode. As shown in Figure S1b in the Supporting Information, porous carbon nanofibers (denoted PCNFs) exhibited continuous and interconnected structure with average diameter of ≈300 nm. High resolution transmission electron microscopy (HRTEM) characterization (Figure S2, Supporting Information) also demonstrated the nanoporous structure of PCNFs. We also prepared C/S and C/S/BTO electrodes by heating the mixture of sulfur powder with PCNFs and C/$BaTiO_3$ electrodes, respectively. No S residues were found on the surface of C/S and C/S/BTO nanofibers (Figure 1b,c). The corresponding elemental mapping is also suggesting the uniform distribution of S, C, and N elements in C/S nanofibers (Figure S3, Supporting Information). As compared to C/S and C/S/BTO nanofibers, CSB@$TiO_2$ nanofibers (Figure 1d) did not have any obvious change on the surface or diameter (Figure S4, Supporting Information). Therefore, transmission electron microscopy (TEM) technique was applied to further investigate the surface variation of the CSB@$TiO_2$ nanofibers. As depicted in Figure 1e, several $BaTiO_3$ nanoparticles are well dispersed in the matrix. Besides, ≈4 nm thickness of $TiO_2$ nanolayers (Figure 1f) grown on the surface of the nanofibers can be clearly observed. To further credibly confirm the thickness of $TiO_2$ layer, electron energy loss spectroscopy (EELS) maps of the CSB@$TiO_2$ composite are shown in Figure S5 in the Supporting Information, the Ti and O signals are strongest near the edges of the imaged area, where the signals are mainly originating from the $TiO_2$ shell. Combining with TEM and elemental mapping analysis, it is confirmed the homogeneous distribution of elements (C, S, Ti, and N) (Figure 1h) with the 1D carbon matrix as well as the uniform $TiO_2$ deposition. Furthermore, such free-standing electrodes can be easily tailored into favorite shapes (square and circular), displaying a good flexibility, as demonstrated in Figure 1g.

Further, we investigated the structural changes of different samples before and after sulfur impregnation and $TiO_2$ ALD treatment through characterization. The X-ray diffraction (XRD) patterns of the bare sulfur, $BaTiO_3$ nanoparticles, PCNFs, C/S, C/S/BTO, and CSB@$TiO_2$ samples were recorded. All the strong reflections of C/S/BTO and CSB@$TiO_2$ electrodes attributed to the $BaTiO_3$, as shown in **Figure 2**a. However, the amplified patterns of the C/S, C/S/BTO, and CSB@$TiO_2$ composites also showed several small peaks, which should be ascribed to the S signal and demonstrating a weak crystalline state of the S.[54,55] On the other hand, the reflections belong to the $TiO_2$ nanolayers could not be detected probably due to their trace amount and amorphous structure.[31] The weight percentage of S and $BaTiO_3$ additive in the electrodes were estimated by

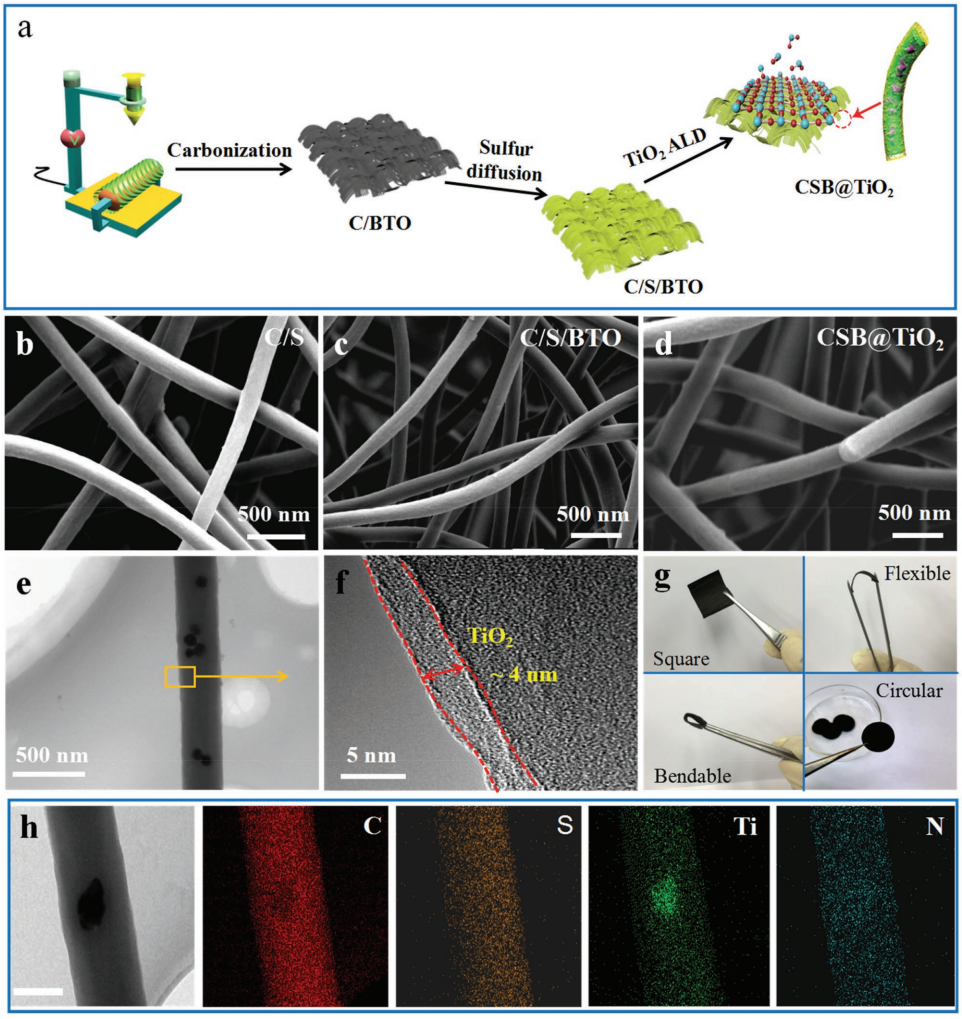


**Figure 1.** a) Schematic illustration of the CSB@$TiO_2$ electrode preparation process. FESEM images of the b) C/S, c) C/S/BTO, and d) CSB@$TiO_2$ electrodes. e,f) TEM images of the CSB@$TiO_2$ nanofiber. g) Photograph of the CSB@$TiO_2$ free-standing electrode, and h) the corresponding elemental mapping images of C, S, Ti, and N elements of the CSB@$TiO_2$ nanofiber. Scale bar: 200 nm.

thermogravimetric (TG) analysis (Figure 2b). The amount of the $BaTiO_3$ additive is about 3 wt% by comparing the TG results of C/S and C/S/BTO electrodes, and 65, 62, and 60 wt% of the sulfur contents calculated for C/S, C/S/BTO, and CSB@$TiO_2$ electrodes, respectively. In order to confirm whether any sulfur coating on the C surface, the elemental line scan test was also conducted. As shown in Figure S6 in the Supporting Information, compared with the C element, S element seems to perform a higher content on the surface after eliminating the influence of the carbon film on TEM copper grid, which demonstrates the possibility of some sulfur coating on the carbon surface. Besides, ≈2 wt% of mass lost after $TiO_2$ deposition due to $TiO_2$ nanolayer additive and the loss the sulfur during the ALD process.[31] Nitrogen adsorption–desorption measurements were also conducted to measure the surface area and pore size in Figure 2c. The pore size of PCNFs electrode (inset of Figure 2c) is mainly concentrated at the range of 1–3 nm while almost disappeared after the sulfur infusion and $TiO_2$ ALD process. The Brunauer–Emmett–Teller surface area decreased from 589 $m^2\ g^{-1}$ for PCNFs to 18 and 14 $m^2\ g^{-1}$ for C/S and CSB@$TiO_2$ electrodes, respectively, indicating the well distributing of S into the porous carbon nanofiber matrix.

To further investigate the comparison of PCNFs, C/S, C/S/BTO, and CSB@$TiO_2$ electrodes, Raman spectroscopy measurements were performed as shown in Figure 2d. For the sulfur powder, there exists three obvious peaks located at 474, 221, and 165.6 $cm^{-1}$, respectively, which are assigned to the characteristic peaks of S—S bonding vibration of $S_8$ molecule. The amplified patterns of the C/S, C/S/BTO, and CSB@$TiO_2$ composites also showed small peak at 221 $cm^{-1}$, which should be ascribed to the S signal. It is verifying that sulfur is stored with weak crystalline order and fully mixed in the carbon material.[7,54,55] Furthermore, all of the samples exhibited similar peaks located at around 1357 and 1596 $cm^{-1}$, which can be assigned to the D bands of disordered $sp^3$ and G bands of graphitic $sp^2$ stretching. It can be seen that the S impregnation and $TiO_2$ deposition showed almost no influence the $I_D/I_G$ ratio. The chemical composition and chemical bonds of the C/S and CSB@$TiO_2$ electrodes were also studied by X-ray photoelectron spectroscopy (XPS) measurements. As compared with the C/S electrode, full spectra

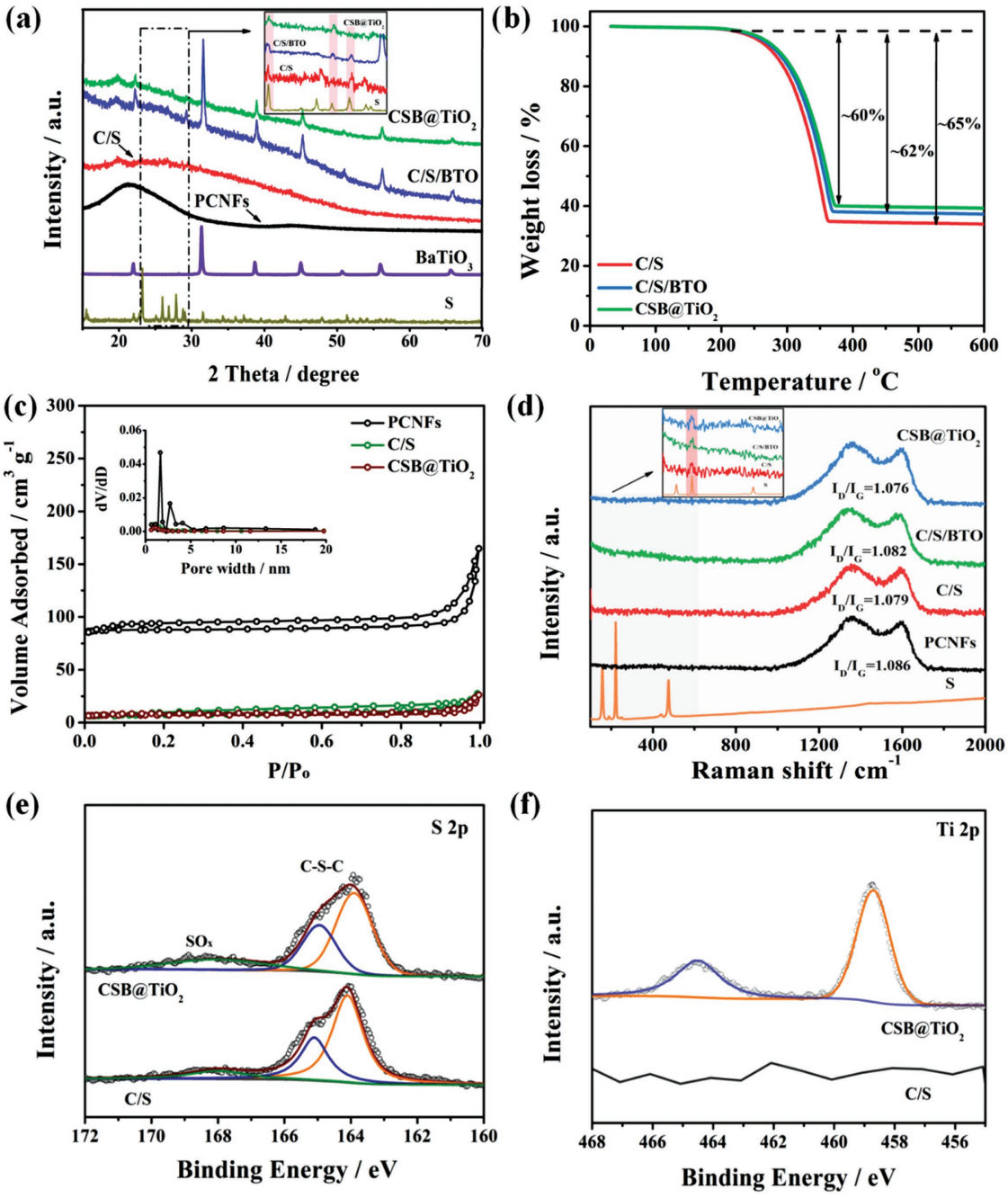


**Figure 2.** a) XRD patterns of the bare $BaTiO_3$ nanoparticles, PCNFs, C/S, C/S/BTO, and CSB@$TiO_2$ electrodes. b) TG curves of the C/S, C/S/BTO, and CSB@$TiO_2$ electrodes. c) $N_2$ adsorption–desorption isotherms and the corresponding pore size distribution of PCNFs, C/S, and CSB@$TiO_2$ electrodes. d) Raman spectra of PCNFs, C/S, C/S/BTO, and CSB@$TiO_2$ electrodes. High-resolution e) S 2p and f) Ti 2p XPS spectrum of the C/S and CSB@$TiO_2$ electrodes.

(Figure S7, Supporting Information) reveal the coexistence of Ti and O elements for the CSB@$TiO_2$ electrode due to the $TiO_2$ nanolayers. For C 1s XPS spectra (Figure S8a, Supporting Information), two peaks have been identified for C/S and CSB@$TiO_2$ samples, corresponding to the $sp^3$ C peak (C—C/C=C, located at 284.7 eV) and $sp^3$ C peak (C—S/C—O, located at 285.9 eV), respectively. For S 2p XPS spectra (Figure 2e), three peaks are detected at around 164, 165, and 168 eV, which are mainly contributed to the bond of S $2p_{3/2}$, $2p_{1/2}$ (C—S—C), and S=O, respectively.[14,17,23] The clear difference has been observed in XPS spectra of C/S and CSB@$TiO_2$ electrodes (Figure 2f) due to deposition of $TiO_2$ on the surface of C/S/BTO nanofibers, which is consistent with TEM analysis. Besides, the deconvolution of N signals for CSB@$TiO_2$ composite is also conducted (Figure S8b, Supporting Information). Three main peaks located at 398.2, 400.1, and 400.9 eV were related to pyridinic-, pyrrolic-, and

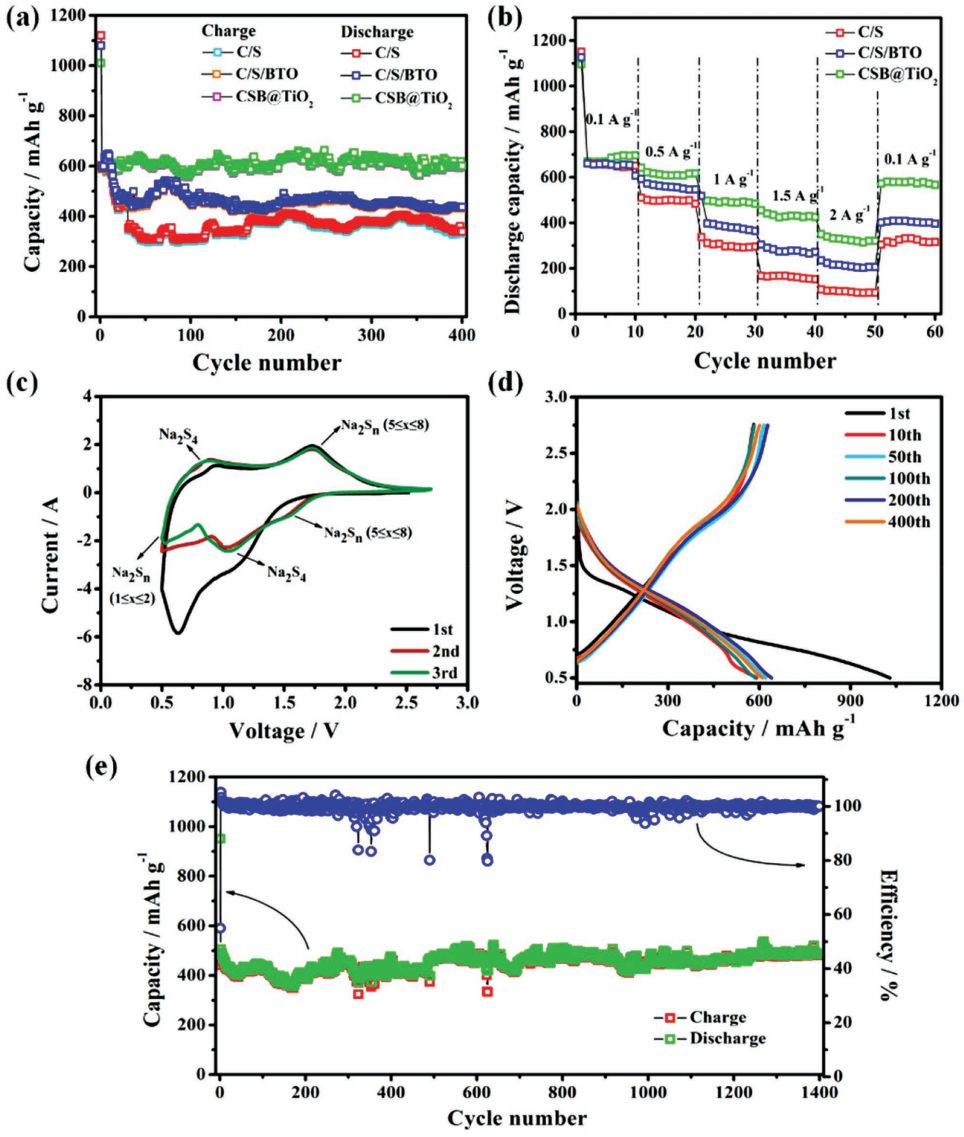


**Figure 3.** a) Cycling performance of C/S, C/S/BTO, and CSB@$TiO_2$ electrodes at 0.5 A $g^{-1}$. b) Rate capability of C/S, C/S/BTO, and CSB@$TiO_2$ electrodes at varied current density from 0.1 to 0.5, 1, 1.5, and 2 A $g^{-1}$. c) The CV curves of CSB@$TiO_2$ electrode in the first three cycles. d) Charge/discharge curves of CSB@$TiO_2$ electrode at 0.5 A $g^{-1}$ in the first, 10th, 50th, 100th, 200th, and 400th cycles. e) The long-term cycling of CSB@$TiO_2$ electrode after 1400 cycles at 1 A $g^{-1}$.

quaternary-N, respectively, which would enhance the electronic conductivity of the carbon matrix during cycling.[19,31]

**Figure 3**a shows the cycling performance of C/S, C/S/BTO, and CSB@$TiO_2$ electrodes at 0.5 A $g^{-1}$ in voltage range from 0.5 to 2.7 V. Discharge capacity of the first two cycles are 1120 and 601 mA h $g^{-1}$, for C/S, 1101 and 621 mA h $g^{-1}$ for C/S/BTO, 1020 and 592 mA h $g^{-1}$ for CSB@$TiO_2$, respectively. As the cycling continued, the capacity of C/S gradually decayed, reached to 310 mA h $g^{-1}$ at 50th cycle. On the contrary, C/S/BTO electrode displays an improvement of performance due to the $BaTiO_3$ additive. Surprisingly, with the $TiO_2$ ALD treatment, CSB@$TiO_2$ electrode has shown better stability with a discharge capacity of 611 mA h $g^{-1}$ after 400 cycles. This is much higher than 340 and 459 mA h $g^{-1}$ for C/S and C/S/BTO electrodes, respectively. As the carbon matrix, PCNFs mat was also used as electrode, it only showed a discharge capacity of 67.6 mA h $g^{-1}$ after 200 cycles at 0.5 A $g^{-1}$ (Figure S9, Supporting Information). The additional cycling performance at a current density of 0.5 A $g^{-1}$ based on the higher loading level of about 3.3–3.5 mg $cm^{-2}$ of electrode is shown in Figure S10 in the Supporting Information. The discharge capacity of the first two cycles are 1055 and 454 mA h $g^{-1}$, for C/S, 1040 and 513 mA h $g^{-1}$ for C/S/BTO, 967 and 587 mA h $g^{-1}$ for CSB@$TiO_2$, respectively. Similar with the result in Figure 3a, the capacity of C/S gradually decayed and reached to 307 mA h $g^{-1}$ after 120 cycles. On the contrary, C/S/BTO electrode displays a partial improvement of performance. For CSB@$TiO_2$ electrode, it still performed the highest stability with a discharge capacity of 559 mA h $g^{-1}$ after 120 cycles with a Coulombic efficiency of 95.1% based on the 2th cycle. This value is much

higher than that of 67.6% and 83.7% for C/S and C/S/BTO composite, respectively. The efficiency of $TiO_2$ nanolayers was evidenced by the change in the rate capabilities. Figure 3b compares the rate capability of C/S, C/S/BTO, and CSB@$TiO_2$ electrodes at current densities at 0.1, 0.5, 1, 1.5, and 2 A $g^{-1}$. The CSB@$TiO_2$ electrode displayed better rate of performance with higher specific capacity, varying from 671 to 622.5, 518, 455, and 350 mA h $g^{-1}$, respectively as compared to other two electrodes. Remarkably, when the current density turns back to 0.1 A $g^{-1}$ after 50 cycles, the reversible capacity recovered to 580 mA h $g^{-1}$ with a retention of 86.4%, which is higher than 47.6% and 60.2% for C/S and C/S/BTO electrodes, respectively.

The CSB@$TiO_2$ electrode was directly used as cathodes, assembled into coin cells with the common carbonate-based electrolyte (ethylene carbonate/diethyl carbonate (EC/DEC)-1M $NaClO_4$). Then the first three cyclic voltammetry (CV) profiles were recorded from 0.5 to 2.7 V at a scan rate of 0.1 mV $s^{-1}$. As indicated in Figure 3c, the wide peak from 2.7–1 V in the initial discharge process should be ascribed to the gradual transition from long-chain $Na_2S_n$ ($5 \le n \le 8$) to short-chain $Na_2S_4$, while the sharp peak at 0.64 V likely corresponds to the further transition from $Na_2S_4$ to $Na_2S_2$, and $Na_2S$, as well as the formation of solid state interface (SEI) layer. Afterward two peaks over the corresponding anodic scan should be ascribed to the oxidation of short-chain sodium sulfides into long-chain polysulfides, while at 0.92 V is for $Na_2S_4$ and at 1.73 V is for $Na_2S_n$ ($5 \le n \le 8$), respectively. For the subsequent cathodic scan, three repeatable peaks at 1.56 V (i.e., the formation of $Na_2S_n$ ($5 \le n \le 8$)), 1.06 V (i.e., the formation of $Na_2S_4$) and 0.53 V (i.e., the formation of $Na_2S_n$ ($1 \le n \le 2$)) (vs $Na/Na^+$) are observed over the 2nd and 3rd cycles, demonstrating the good cycling stability of the CSB@$TiO_2$ electrode.[11] Similar discharge/charge behaviors were also observed for C/S and C/S/BTO electrodes (Figure S11, Supporting Information). Compared with the C/S electrode, C/S/BTO, and CSB@$TiO_2$ electrodes performed a better reversibility due to the good overlap after 1st cycle. Besides, the potential interval of the redox peak ascribed to $Na_2S_4$ were calculated to be 0.23 V for C/S/BTO electrode and 0.14 V for CSB@$TiO_2$ electrode, which indicates a lower polarization benefited from the $TiO_2$ protective layer. The discharge and charge profiles of CSB@$TiO_2$ electrode at 0.5 A $g^{-1}$ within the voltage range of 0.5–2.7 V are presented in Figure 3d. The almost overlapping curves from 1st to 400th cycles demonstrated the stable reaction interface and weak polarization of the CSB@$TiO_2$ sample.

Normally, long-cycling lifespan is an essential requirement for energy storage devices in practical application. Figure 3e shows the long-term charge/discharge test for CSB@$TiO_2$ electrode at 1 A $g^{-1}$, and first two discharge capacities of 952 and 498 mA h $g^{-1}$ were achieved, respectively. Remarkably, a discharge capacity of 524.8 mA h $g^{-1}$ was achieved after 1400 cycles, with retention of 105.4% based on the 2th cycle. Moreover, such electrode maintained a capacity of 382 mA h $g^{-1}$ even after 3000 cycles with a Coulombic efficiency of 106.1% based on the 2th cycle at a current density of 2 A $g^{-1}$ (Figure S12, Supporting Information). To the best of our knowledge, this is the best cyclic stability results of RT Na–S batteries using carbonate-based electrolyte when comparing with the previous reports (i.e., the normal reported lifespan is less than 500 cycles, while we extend it to 1400, and even 3000 cycles) (Table S1, Supporting Information).

To demonstrate the stable long-term cycling performance of the electrodes, cell impedance of the C/S and CSB@$TiO_2$ electrodes in the full charge state after 10th, 100th, 200th, and 400th cycles have been conducted by electrochemical impedance spectroscopy (EIS), as shown in **Figure 4**a,b, respectively. Similar to the Li–S batteries, the Nyquist plot of Na–S batteries contained a depressed semicircle in the high-to-middle frequency region and a sloped line in the low-frequency range, corresponding to the charge-transfer resistance ($R_{ct}$) and Warburg impedance, respectively.[31,33,38] All the results were fitted according to the equivalent circuits (Figure S13, Supporting Information) and summarized (Table S2, Supporting Information). Additionally, the values of $R_{ct}$ for C/S and CSB@$TiO_2$ electrodes are calculated in Figure 4c. Obviously, the C/S electrode showed a huge increment from 175.6 Ω (10th) to 1024 Ω (400th ) as compared to CSB@$TiO_2$ electrode from 183.4 to 497 Ω. Compared with the C/S and C/S/BTO electrodes, CSB@$TiO_2$ displayed a rigid structure without any structural damage after 200 cycles as represented in Figure S14 in the Supporting Information. Combined with the EIS tests and morphology observations, the superior electrochemical of CSB@$TiO_2$ composite achieved by the deposition of $TiO_2$ protective layer was presented in Figure 4d. The $TiO_2$ protective layer renders the structural integrity of electrode by suppressing the volume changes during charge/discharge process. On the other hand, the $TiO_2$ protective layer also reduces the interfacial resistance, facilitating the charge transfer and ionic transport, therefore improving the rate of capability.

To investigate the solubility of intermediate phases during cycling, five cycled electrodes of C/S, C/S/BTO, and CSB@$TiO_2$ at different charge/discharge state were immersed into carbonate electrolyte for 10 d. The color of solution was changed to yellow for C/S (**Figure 5**a), faint yellow for C/S/BTO (Figure S15, Supporting Information), and almost no color change for CSB@$TiO_2$ (Figure 5b). Such observation indicates the effective adsorption ability of $TiO_2$ layer toward polysulfides. Furthermore, the UV–vis spectra (Figure S16, Supporting Information) also demonstrated the existence of $S_3^{2-}/S_6^{2-}$ and $S_4^{2-}/S_6^{2-}$, and the weak UV–vis absorbance for polysulfides also indicates the good adsorption ability from the $TiO_2$ layer.[56–58] In addition, the similar phenomenon (Figure S17, Supporting Information) is also observed and received similar UV–vis results (Figure S18, Supporting Information) when the loading mass of electrodes were increasing to about 3.3–3.5 mg $cm^{-2}$. To further explore the stability of $TiO_2$ deposited nanolayer, cycled CSB@$TiO_2$ electrode at full discharge state was also characterized by field emission scanning electron microscopy (FESEM) test. As shown in Figure 5c, the CSB@$TiO_2$ nanofibers still have interconnected structure, and corresponding energy dispersive X-ray spectroscopy (EDS) mapping distribution of C, Na, Ti, and O elements were also consistent with the original sample, demonstrating a rigid and uniform $TiO_2$ deposition.

As result, the mechanism of the CSB@$TiO_2$ composites also proposed in Figure 5d,e. For C/S/BTO composite, the hetero polar polysulfides enable to be absorbed by the internal electric field originated from the spontaneous polarization of $BaTiO_3$ nanoparticles, thus receiving an improved cycling stability compared with the C/S composite. However, such strategy would

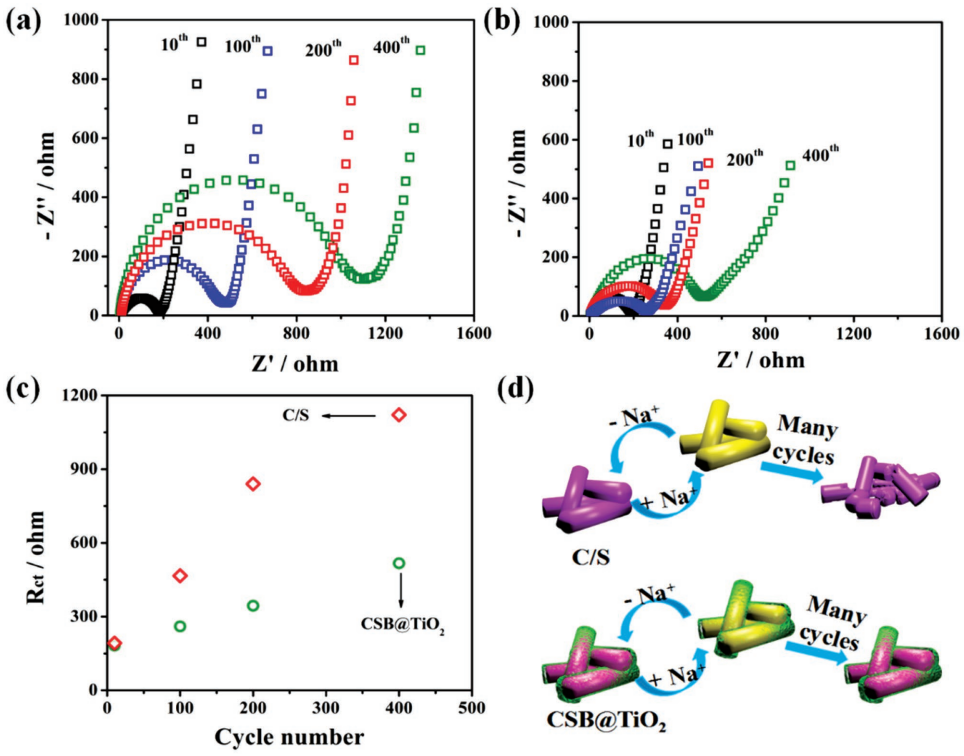


**Figure 4.** Cell impedance tests of the a) C/S and b) CSB@$TiO_2$ electrodes in the full charge state after the 10th, 100th, 200th, and 400th cycles. c) The comparison of C/S and CSB@$TiO_2$ electrodes about the charge transfer resistance. d) The proposed stabilizing effect of $TiO_2$ nanolayer deposition on the C/S/BTO composites.

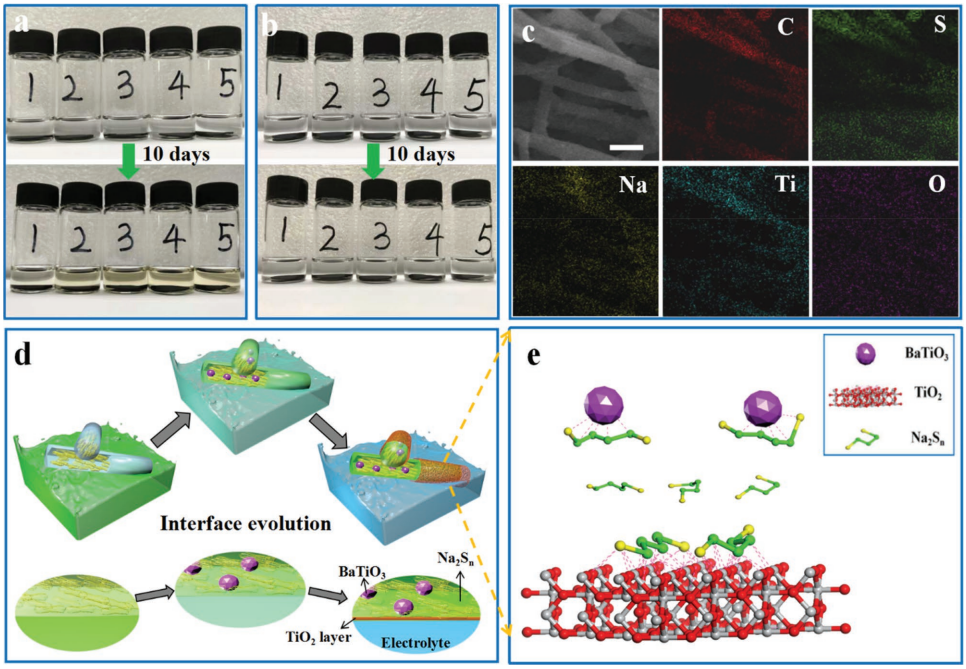


**Figure 5.** Photograph of the carbonate-based electrolyte with the a) C/S and b) CSB@$TiO_2$ electrodes charged to (1) 0.8, (2) 1.7 V, discharged to (3) 2.0, (4) 1.7, (5) 1.0 V after 10 d. c) FESEM images of the 400th cycled CSB@$TiO_2$ electrode at full discharge state and the corresponding elemental mapping images of C, Na, Ti, and O. Scale bar: 500 nm.d,e) The proposed synergistic effect of $BaTiO_3$ additive and $TiO_2$ layer deposition for ultrastable CSB@$TiO_2$ electrode.

inevitably lead to the dissolution of polysulfide distributed near the electrolyte due to their weak interaction with $BaTiO_3$ nanoparticles. The $TiO_2$ nanolayers were thus deposited on the surface of C/S/BTO nanofibers to form "$BaTiO_3$-C-$TiO_2$" composite. Such unique architecture enables to provide a stable $Na^+$ transport interface, trapping and confining the intermediate polysulfide inside the carbon matrix to the greatest extent during cycling, and achieving an excellent electrochemical performance.

## 3. Conclusion

In summary, for achieving high energy density and low cost of RT Na–S batteries, we have developed a new strategy based on the synergistic effect resulted from only ≈3 wt% of $BaTiO_3$ additive and ≈4 nm thickness of amorphous $TiO_2$ ALD protective layer. The half-cell combined with CSB@$TiO_2$ cathode displayed better rate capability than both of C/S and C/S/BTO electrodes. For cycling performance, this CSB@$TiO_2$ electrode performed discharge capacity of 611 mA h $g^{-1}$ after 400 cycles at 0.5 A $g^{-1}$, compared with 340 and 459 mA h $g^{-1}$ of C/S and C/S/BTO electrodes, respectively. Notably, the CSB@$TiO_2$ electrode remained at 524.8 mA h $g^{-1}$ after 1400 cycles at 1 A $g^{-1}$ and 382 mA h $g^{-1}$ after 3000 cycles at 2 A $g^{-1}$, respectively. Such ultrastable CSB@$TiO_2$ electrodes used for Na–S batteries should be beneficial from the "$BaTiO_3$-C-$TiO_2$" interactive components, which inhibiting the volume expansion, improving the utilization of active material, and ensuring stable ionic transport interface. Our finding here tends to take advantages of the combining benefits of ALD modification and additive with small amount, which may be a rational way for designing other new materials for high performance and inexpensive metal-sulfur batteries.

## 4. Experimental Section

*Preparation of the Porous C/$BaTiO_3$ Nanofibers*: The porous C/$BaTiO_3$ nanofibers were synthesized by using electrospinning technique and following carbonization. Typically, 1.4 g of polyacrylonitrile, 50 mg of F127 and 30 mg of $BaTiO_3$ were dissolved into 15 mL of dimethylformamide solvent and stirred for 20 h to form a homogeneous spinning solution. Then, the obtained solution was loaded into a 25 mL of syringe pump, and the electrospinning process was operated at applied voltage of 14.5 kV, feeding rate of 1.5 mL $h^{-1}$, as well as collected distance of 15 cm. Finally, nonwoven film could be easily peeled off from the aluminum foil and successively dried at 80 °C under vacuum overnight. With regard to the carbonization process, dried film was first stabilized at 280 °C for 4 h in air, then carbonized at 900 °C for another 6 h at 2 K $min^{-1}$ heating rate under $N_2$ atmosphere.

*Preparation of the C/S/$BaTiO_3$ Nanofibers*: The porous C/$BaTiO_3$ mats were punched to disc with a 0.6 cm radius and mixed with sulfur powder. Subsequently, they were heated to 160 °C for 10 h under vacuum and then raised to 260 °C for 1 h in an Ar-filled tubular furnace to yield the C/S/$BaTiO_3$ composite (denoted C/S/BTO).

*Preparation of the (C/S/$BaTiO_3$)@$TiO_2$ Composite*: The $TiO_2$ protective layer was directly grown on the free-standing C/S/$BaTiO_3$ electrode using KE-MICRO PEALD-200A machine under $4 \times 10^{-3}$ torr at 140 °C. Typically, titanium tetraisopropanolate (TTIP, Fornano, 99.9999%) and deionized $H_2O$ were used as the titanium and oxygen source, respectively. Ar (99.999%) gas was used as the carrier gas with a flow rate of 20 sccm. Typically, a complete ALD cycle consisting of a sequential and alternating supply of TTIP and $H_2O$ as follows: a 0.2 s supply of TTIP vapor, a 7 s exposure to the electrodes, a 50 s-Ar purge, a 0.1 s supply of water vapor, a 7 s extended exposure to the electrodes, and 60 s-Ar purge. The ALD processes were conducted for 30 layers to produce the (C/S/$BaTiO_3$)@$TiO_2$ composites (denoted CSB@$TiO_2$). Notably, it should be pointed out that the content of $TiO_2$ was difficult to be accurately measured in the composite due to its ultrasmall amount.

*Characterizations*: The morphology and microstructure of the samples were examined by FESEM (JSM-7800F & TEAM Octane Plus) and HRTEM (Tecnai G2 F30). The structure and Raman spectra were collected on X-ray diffraction (Bruker, D8 Advance with Cu-Ka radiation) and Raman microscope (DXR Thermo-Fisher Scientific), respectively. Thermogravimetric analysis (TGA-Q50) was performed under nitrogen atmosphere from room temperature up to 600 °C with a heating rate of 10 °C $min^{-1}$. BELSORP-max Surface Area and Porosimetry instrument was used to measure the nitrogen adsorption/desorption isotherms of electrodes. XPS tests were carried out using an ESCALAB 250Xi system, all data were calibrated using adventitious C1s peak at a fixed value of 284.4 eV.

*Electrochemical Measurements*: The electrochemical tests were performed with CR2032 coin-type batteries, which were assembled with sodium metal as the counter and reference electrodes inside an argon-filled glove box (MBRAUN, UNILab2000, both moisture and oxygen level below 1 ppm). Glass fiber (Whatman) was used as the separator. The electrolyte was 1 M of $NaClO_4$ in a mixture of EC and DEC (1:1 v/v). The free-standing samples were directly used as the working electrode without any other additives. The loading mass of active material was 1.2–1.4 mg $cm^{-2}$. The galvanostatic charge–discharge tests were carried out over a voltage range of 0.5–2.7 V (vs $Na^+$/Na) on a battery test system (Land, CT-2001A). EIS measurements were performed using the electrochemical workstation (CHI760D) by applying a voltage of 5 mV over a frequency of $10^{-2}$–$10^5$ Hz. All the cells were held at ambient temperature for at least 8 h before tests. All the specific capacity was calculated based on the sulfur mass loading.

## Supporting Information

Supporting Information is available from the Wiley Online Library or from the author.

## Acknowledgements

D.T.M. and Y.L.L. contributed equally to this work. This work was financially supported by the National Natural Science Foundation of China (Nos. 51774203, 51374146, 51502177), the Foundation of Guangdong Educational Committee (No. 2016KTSCX124), Shenzhen Science and Technology Project Program (Nos. ZDSYS201606061530079, KQJSCX20170327151152722, JCYJ20160422112012739), the National Natural Science Foundation of SZU (827-000039).

## Conflict of Interest

The authors declare no conflict of interest.

## Keywords

$BaTiO_3$, ferroelectric-encapsulated cathodes, free-standing batteries, room temperature sodium–sulfur batteries, $TiO_2$

Received: September 24, 2017
Revised: December 3, 2017
Published online:

[1] A. Manthiram, Y. Fu, Y. Su, *Acc. Chem. Res.* **2013**, *5*, 1125.
[2] R. Fang, S. Zhao, Z. Sun, D. Wang, H. Cheng, F. Li, *Adv. Mater.* **2017**, *29*, 1606823.
[3] Q. Pang, X. Liang, C. Y. Kwok, L. F. Nazar, *Nat. Energy* **2016**, *1*, 132.
[4] Y. Yin, S, Xin , Y. Guo, L. Wan, *Angew. Chem., Int. Ed.* **2013**, *52*, 13186.
[5] S. Wei, S. Xu, A. Agrawral, S. Choudhury, Y. Lu, Z. Tu, L. Ma, L. Archer, *Nat. Commun.* **2016**, *7*, 11722.
[6] A. Manthiram, X. Yu, *Small* **2015**, *18*, 2108.
[7] R. Carter, L. Oakes, A. Douglas, N. Muralidharan, A. Cohn, C. Pint, *Nano Lett.* **2017**, *3*, 1863.
[8] J. Wang, J. Yang, Y. Nuli, R. Holze, *Electrochem. Commun.* **2007**, *1*, 31.
[9] T. H. Hwang, D. S. Jung, J. Kim, B. Kim, J. Choi, *Nano Lett.* **2013**, *9*, 4532.
[10] Y. Chen, W. Liang, S. Li, F. Zou, S. Bhaway, Z. Qiang, M. Gao, B. Vogt, Y. Zhu, *J. Mater. Chem. A* **2016**, *32*, 12471.
[11] Y. Wang, J. Yang, W. Lai, S. Chou, Q. Gu, H. Liu, D. Zhao, S. Dou, *J. Am. Chem. Soc.* **2016**, *51*, 16576.
[12] S. Xin, Y. Yin, Y. Guo, L. Wan, *Adv. Mater.* **2014**, *8*, 1261.
[13] Q. Lu, X. Wang, J. Cao, C. Chen, K. Chen, Z. Zhao, Z. Niu, J. Chen, *Energy Storage Mater.* **2017**, *8*, 77.
[14] L. Fan, R. Ma, Y. Yang, S. Chen, B. Lu, *Nano Energy* **2016**, *28*, 304.
[15] L. Zeng, Y. Yao, J. Shi, Y. Jiang, W. Li, L. Gu, Y. Yu, *Energy Storage Mater.* **2016**, *5*, 50.
[16] Y. Yao, L. Zeng, S. Hu, Y. Jiang, B. Yuan, Y. Yu, *Small* **2017**, *19*, 1603513.
[17] I. Bauer, M. Kohl, H. Althues, S. Kaskel, *Chem. Commun.* **2014**, *24*, 3208.
[18] S. Zheng, P. Han, Z. Han, P. Li, H. Zhang, J. Yang, *Adv. Energy Mater.* **2014**, *12*, 1400226.
[19] M. Kohl, F. Borrmann, H. Althues, S. Kaskel, *Adv. Energy Mater.* **2016**, *6*, 1502185.
[20] X. Liu, J. Q. Huang, Q. Zhang, L. Mai, *Adv. Mater.* **2017**, *20*, 1601759.
[21] S. Xin, L. Gu, N. Zhao, Y. Yin, L. Zhou, Y. Guo, L. Wan, *J. Am. Chem. Soc.* **2012**, *45*, 18510.
[22] G. He, S. Evers, X. Liang, M. Cuisinier, A. Garsuch, L. F. Nazar, *ACS Nano* **2013**, *12*, 10920.
[23] Y. Zhang, Z. Wu, G. Pan, S. Liu, X. Gao, *ACS Appl. Mater. Interfaces* **2017**, *14*, 12436.
[24] X. Zhao, H. J. Ahn, K. W. Kim, K. K. Cho, J. H. Ahn, *J. Phys. Chem. C* **2015**, *15*, 7996.
[25] M. Agostini, S. Xiong, A. Matic, J. Hassoun, *Chem. Mater.* **2015**, *13*, 4604.
[26] S. Je, T. Hwang, S. N. Talapaneni, O. Buyukcakir, H. Kim, J. Yu, S. G. Woo, M. C. Jang, B. Son, A. Coskun, J. W. Choi, *ACS Energy Lett.* **2016**, *3*, 566.
[27] W. Zhou, Y. Yu, H. Chen, F. J. DiSalvo, H. D. Abruña, *J. Am. Chem. Soc.* **2013**, *44*, 16736.
[28] Q. Pang, D. Kundu, L. F. Nazar, *Mater. Horiz.* **2016**, *3*, 130.
[29] S. Zhang, D. T. Tran, *J. Mater. Chem. A* **2016**, *4*, 4371.
[30] Y. Lu, X. Li, J. Liang, L. Hu, Y. Zhu, Y. Qian, *Nanoscale* **2016**, *8*, 17616.
[31] M. Yu, J. Ma, H. Song, A. Wang, F. Tian, Y. Wang, H. Qiu, R. Wang, *Energy Environ. Sci.* **2016**, *4*, 1495.
[32] J. Li, M. Zhu, P. Hu, X. Wang, L. Zhang, M. Li, *Eur. J. Inorg. Chem.* **2017**, *26*, 3248.
[33] X. Zhao, H. Wang, G. Zhai, G. Wang, *Chem. Eur. J.* **2017**, *29*, 7037.
[34] Z. Li, J. Zhang, X. W. Lou, *Angew. Chem., Int. Ed.* **2015**, *44*, 12886.
[35] S. Rehman, T. Tang, Z. Ali, X. Huang, Y. Hou, *Small* **2017**, *20*, 1700087.
[36] L. Zhou, N. Ding, J. Yang, L. Yang, Y. Zong, Z. Liu, A. Yu, *ACS Sustainable Chem. Eng.* **2016**, *7*, 3679.
[37] J. He, L. Luo, Y. Chen, A. Manthiram, *Adv. Mater.* **2017**, *29*, 1702707.
[38] H. A. Salem, V. R. Chitturi, G. Babu, J. A. Santana, D. Gopalakrishnan, L. M. Arava, *RSC Adv.* **2016**, *6*, 110301.
[39] L. Carbone, S. G. Greenbaum, J. Hassoun, *Sustainable Energy Fuels* **2017**, *1*, 228.
[40] X. H. Cao, C. L. Tan, M. Sindoro, H. Zhang, *Chem. Soc. Rev.* **2017**, *46*, 2660.
[41] Z. Xiao, Z. Yang, L. Wang, H. Nie, M. Zhong, Q. Lai, X. Xu, L. Zhang, S. Huang, *Adv. Mater.* **2015**, *27*, 2891.
[42] Z. Zhang, Y. Lai, Z. Zhang, K. Zhang, J. Li, *Electrochim. Acta* **2014**, *129*, 55.
[43] T. Zhao, Y. Ye, X. Peng, G. Divitini, H. K. Kim, C. Y. Lao, P. R. Coxon, K. Xi, Y. J. Liu, C. Ducati, R. Chen, R. V. Kumar, *Adv. Funct. Mater.* **2016**, *46*, 8418.
[44] Y. Mi, W. Liu, K. Yang, J. Jiang, Q. Fan, Z. Weng, Y. Zhong, Z. Wu, G. W. Brudvig, V. S. Batista, H. Zhou, H. Wang, *Angew. Chem., Int. Ed.* **2016**, *47*, 14818.
[45] L. Jia, T. Wu, J. Lu, L. Ma, W. Zhu, X. Qiu, *ACS Appl. Mater. Interfaces* **2016**, *44*, 30248.
[46] Q. Fan, W. Liu, Z. Weng, Y. Sun, H. Wang, *J. Am. Chem. Soc.* **2015**, *40*, 12946.
[47] Z. Seh, W. Li, J. Cha, G. Y. Zheng, Y. Yang, M. T. McDowell, P. C. Hsu, Y. Cui, *Nat. Commun.* **2013**, *4*, 1331.
[48] K. Xie, Y. You, K. Yuan, W. Lu, K. Zhang, F. Xu, M. Ye, S. Ke, C. Shen, X. Zeng, X. Fan, B. Wei, *Adv. Mater.* **2017**, *29*, 1604724.
[49] Y. Taeeun, H. Seung, P. Nam, M. Park, J. Lee, J. Shin, J. Choi, Y. Jung, Y. Jo, J. Yu, K. Kim, *Adv. Funct. Mater.* **2016**, *26*, 7817.
[50] T. Teranishi, Y. Yoshikawa, R. Sakuma, H. Okamura, H. Hashimoto, H. Hayashi, T. Fujii, A. Kishimoto, Y. Takeda, *ECS Electrochem. Lett.* **2015**, *12*, A137.
[51] S. Xiong, J. Fan, Y. Wang, J. Zhu, J. Yu, Z. Hu, *J. Mater. Chem. A* **2017**, *5*, 18242.
[52] Y. Chen, L. Shi, S. Guo, Q. Yuan, X. Chen, J. Zhou, H. Song, *J. Mater. Chem. A* **2017**, *5*, 19866.
[53] W. Libbrecht, A. Verberckmoes, J. W. Thybaut, P. V. D. Voort, J. D. Clercq, *Langmuir* **2017**, *33*, 6769.
[54] H. B. Wu, S. Wei, L. Zhang, R. Xu, H. H. Hng, X. W. Lou, *Chem. Eur. J.* **2013**, *19*, 10804.
[55] C. Zhang, H. B. Wu, C. Yuan, Z. Guo, X. W. Lou, *Angew. Chem., Int. Ed.* **2012**, *51*, 9592.
[56] H. Pan, Z. Cheng, Z. Xiao, X. Li, R. Wang, *Adv. Funct. Mater.* **2017**, *27*, 1703936.
[57] F. Lee, M.-C. Tsai, M.-H. Lin, Y. L. Ni'mah, S. Hy, C.-Y. Kuo, J.-H. Cheng, J. Rick, W.-N. Su, B.-J. Hwang, *J. Mater. Chem. A* **2017**, *5*, 6708.
[58] Y. An, Z. Zhang, H. Fei, S. Xiong, B. Ji, J. Feng, *ACS Appl. Mater. Interfaces* **2017**, *9*, 12400.

 